The Meteoritical Society

Meteoritics & Planetary Science 44, Nr 10, 1445–1463 (2009)
Abstract available online at http://meteoritics.org

Three-dimensional textural and compositional analysis of particle tracks and fragmentation history in aerogel

Denton S. EBEL[1*], Michael GREENBERG[1], Mark L. RIVERS[2], and Matthew NEWVILLE[2]

[1]Department of Earth and Planetary Sciences, American Museum of Natural History, Central Park W. at 79th St., New York 10024, USA
[2]Consortium for Advanced Radiation Sources and Department of the Geophysical Sciences, The University of Chicago, 5640 South Ellis Ave., Chicago, Illinois 60637, USA
[*]Corresponding author. E-mail: debel@amnh.org

(Received 30 June 2009; revision accepted 07 October 2009)

Abstract–We report analyses of aerogel tracks using (1) synchrotron X-ray computed microtomography (XRCMT), (2) laser confocal scanning microscopy (LCSM), and (3) synchrotron radiation X-ray fluorescence (SRXRF) of particles and their paths resulting from simulated hypervelocity impacts (1–2), and a single ~1 mm aerogel track from the Stardust cometary sample collector (1–3). Large aerogel pieces can be imaged sequentially, resulting in high spatial resolution images spanning many tomographic fields of view ('lambda-tomography'). We report calculations of energy deposited, and tests on aromatic hydrocarbons showing no alteration in tomography experiments. Imaging at resolutions from ~17 to ~1 micron/pixel edge (XRCMT) and to <100 nm/pixel edge (LCSM) illustrates track geometry and interaction of particles with aerogel, including rifling, particle fragmentation, and final particle location. We present a 3-D deconvolution method using an estimated point-spread function for aerogel, allowing basic corrections of LCSM data for axial distortion. LCSM allows rapid, comprehensive, non-destructive, high information return analysis of tracks in aerogel keystones, prior to destructive grain extraction. SRXRF with LCSM allows spatial correlation of grain size, chemical, and mineralogical data. If optical methods are precluded in future aerogel capture missions, XRCMT is a viable 3D imaging technique. Combinations of these methods allow for complete, nondestructive, quantitative 3-D analysis of captured materials at high spatial resolution. This data is fundamental to understanding the hypervelocity particle-aerogel interaction histories of Stardust grains.

INTRODUCTION

The Stardust mission (http://stardust.jpl.nasa.gov/home) returned samples of ejecta from comet Wild 2 to earth on 15 January 2006. Particles encountered aerogel tiles at high relative velocity (~6.1 km s^{-1} relative flyby speed), and interacted with aerogel as they slowed down (Tsou et al. 2003). Intense swarms of particles arrived in bursts, consistent with particle fragmentation (Tuzzolino et al. 2004). Fragmentation, sintering and other high-energy events were recorded in the captured particle textures, fragment locations, and track morphologies. Prior to sample recovery, there were concerns that optical methods for reading this record could be compromised by several factors, the worst case included exposure of hygroscopic aerogel to water upon landing. In the actual event, the flight aerogel tiles were recovered dry and in excellent condition for optical examination, such as by microscopy (Westphal et al. 2002; Zolensky 2006). Mission requirements include acquisition of maximum possible information about these samples at all stages of processing.

Synchrotron X-ray computed microtomography (XRCMT) is a non-destructive method for recording the 3-dimensional (3D) density structures of small samples at resolutions as fine as 1 micron/voxel (Ebel et al. 2007; Tsuchiyama et al. 2009). We made tomograms of a partial aerogel tile that was shot with dust from the Allende meteorite on the NASA Ames gas gun (F. Hörz, personal communication). This tile was ~7 mm thick, 40 mm wide, and ~30 mm tall. Our first images had a spatial resolution of ~16 micron per voxel. We then imaged portions of the same sample at ~2.5 micron/voxel. In follow-up work, we imaged the same tile before and after the addition of a few drops of water. Tomography may be useful even if samples are fully accessible to 3D optical methods, but it is certainly the optimal technique if they are not. If samples become wet, track and fragmentation information are likely to be

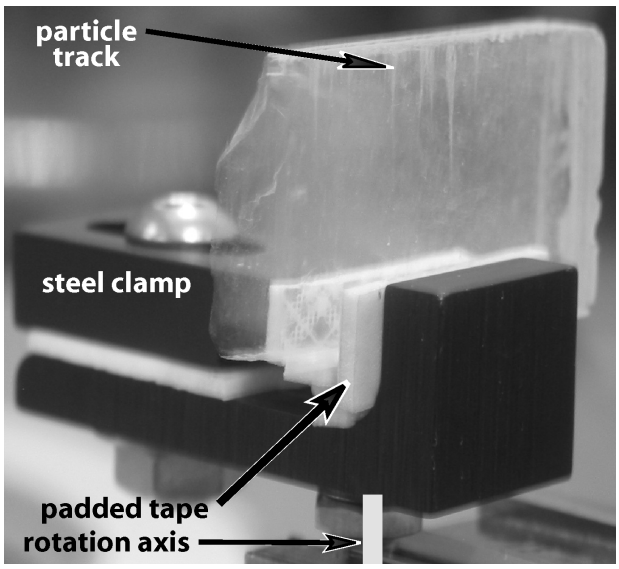

Fig. 1. Aerogel slab in vise, ready for tomography experiment. Rotation axes of individual data sets can be varied in horizontal x-y at will.

completely lost, as most aerogel collapses when subjected to the surface tension of water.

Laser scanning confocal microscopy (LCSM) is an alternative non-destructive method for 3-dimensional mapping of whole tracks of material returned by the Stardust mission. LCSM provides very high contrast reflectance images at a spatial resolution <100 nm per voxel edge in optically transparent samples (Kearsley 2007). Here, we describe procedures for, and demonstrate LCSM images of, track C2092,82 at 0.065 μm/pixel using dry microscopy and analogous images of aerogel shot with basaltic glass, imaged at 0.052 μm/pixel utilizing oil-immersion microscopy techniques. A rigid procedure for 3D image acquisition of Stardust tracks has been described, and will easily transfer to analysis of tracks in the interstellar dust collector.

Axial distortion of 3D images is a serious issue in LCSM, resulting from optical effects along the optic axis of the instrument. We describe basic corrections of axial distortion using a 3-dimensional deconvolution method, based on a theoretical point-spread function (PSF) for aerogel. LCSM data is also used to quantitatively characterize and model the whole of C2092,82 in 3 dimensions. This paper presents a methodology for a suite of rapid and easily accessible nondestructive analysis procedures for complete, high contrast and spatial resolution textural and chemical mapping of whole Stardust tracks in aerogel, and application to track C2092,82 (Track 82).

METHODS

Tomography

X-ray computed microtomography (XRCMT) is the determination of the 3-dimensional density structure of a solid object by computer-assisted reconstruction based on a series of snapshots of the object in X-ray illumination. In two-dimensional (2D) imaging, resolution is described by the size of each picture element, or pixel. In three dimensions (3D), a 'voxel' is a volume element, with an associated single numerical value of the computed X-ray attenuation due to the material in that voxel. Here, voxels are cubes, and spatial resolution is described by the length of voxel edges in micrometers (μm), which correspond to the edges of square pixels in successive slices through the volume (Ebel and Rivers 2007). Previous synchrotron XRCMT studies on aerogel-collected samples include Tsuchiyama et al. (2009) and Nakamura et al. (2008b).

Tomographic analysis was performed on beamline 13BM-D at the Advanced Photon Source (APS; Sutton 2006), Argonne National Labs, U.S. Department of Energy, operated by the University of Chicago through the Geology-Soil-Environmental Consortium for Advanced Radiation Sources (GSE-CARS). A high-flux, high-brilliance synchrotron X-ray beam is maintained at 100 mA in "top-up" mode by constant electron injection. The X-ray beam enters each tangential beamline and is collimated to a single energy before passing through the sample, then a YAG scintillator followed by a 45° mirror to a microscope objective and a high-speed, 12-bit, 1317 × 1035 pixel charge-coupled device (CCD; cf. Ebel and Rivers 2007). Some data was collected by binning the CCD readout by a factor of two in both directions. The beam can be up to 10 mm wide and 4 mm high at the CCD, and allows collection of an entire image at once for every angle of rotation. It is not a point source. The apparatus is configured to allow variation of the distance between the sample and the scintillator-mirror-camera ensemble. A longer distance enhances phase contrast, providing better imaging of boundaries between sample regions with only subtle differences in attenuation.

Each single data set was collected by rotating the sample 0 to 180-ε° in ε° steps, where ε is 1.0, 0.5 or 0.25°. At each angle, a static image (radiogram) was taken, at an exposure time *t* seconds. The sample was removed from the beam, usually every 100th frame, and a white field was collected to enable later correction of the data for variations in the beam. A dark current correction was also applied. Raw data was processed to obtain a 3-dimensional array, or volume, with a 16-bit X-ray attenuation value for each voxel. The volume can be thought of as a stack of virtual, parallel "slices" through the sample. Volume files were reduced significantly in size by cropping to isolate particle tracks. From these fully-processed volume files, stacks of 2D images and movies were generated. To accentuate contrast between features, maximum and minimum grayscale threshold value cutoffs were set, creating 8-bit image and movie files.

Analog Samples

F. Hörz used the gas gun at NASA-AMES Research Center to inject micron-sized particles from the Allende

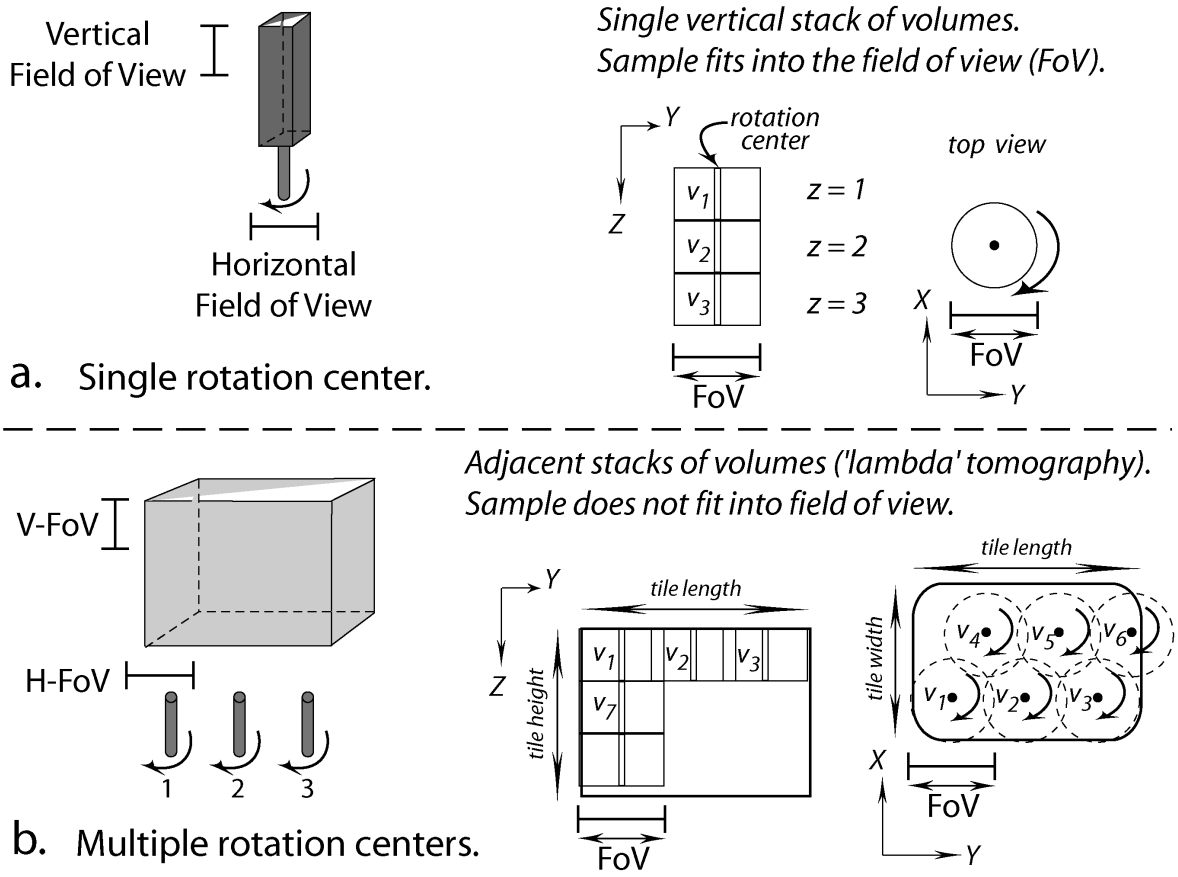

Fig. 2. Schematic of image volume geometries for lambda-tomography.

meteorite into pre-flight, flight-grade aerogel tiles at speeds similar to the 6.1 km s^{-1} expected for the encounter with comet Wild 2. A slab of one such tile was provided for this work. That sample is shown in Fig. 1, clamped in the device used for imaging. This slab is ~7 mm thick, 40 mm wide, and ~30 mm tall. Handling aerogel is difficult due to its sensitivity to static charge and because samples are brittle enough to break into pieces with very little force. In this case, the slab fractured along a diagonal, but the experiment was not compromised.

A new technique was used to image tracks in sub-volumes of the slab. For analysis of aerogel tile at high spatial resolution it is not desirable, nor possible, to cut the sample into very small vertical sticks fitting within the field of view (Tsou et al. 2003; Ebel and Rivers 2007). The very low X-ray attenuation of aerogel, however, makes it possible to penetrate thick samples with relatively low beam energy. Thus it is possible to collect tomographic data sets at very high spatial resolution on adjacent volumes. That is (Fig. 2), portions of the sample can be rotated out of the field of view without significantly affecting our ability to reconstruct the volume of interest to high accuracy. This type of tomography, in which a subset of a large sample is imaged, and portions rotate out of the field of view, has been called "lambda tomography."

Images of portions of the slab were obtained at 12 KeV. Sets of adjacent volumes were obtained for two conditions: 14.49 micron/pixel and 0.7 s/frame, and 3.66 micron/pixel at 1.5 s/frame. In follow-up work, we imaged the same tile after the addition of a few drops of water, at 10 KeV, 11.14 micron/pixel and 2.0 s/frame. This work was done to assess the recoverability of information from wet aerogel, in the event that the water table was high at the time and site of Stardust capsule recovery. For these experiments the detector was set at zero, close to the slab.

In addition to the Allende-shot aerogel slab, we obtained a basalt-shot aerogel keystone containing multiple tracks. In comprehensive testing of analog samples, powdered, unsieved (1–100 μm) USGS Fe-basalt glass standard NKT-1 G (Potts et al. 2005) was shot (5-Dec-06, by Mark Burchell at the U. Kent gas gun) into uniform ρ = 25 kg/m^3 aerogel (average ρ of density-graded flight aerogel) at 5.88 km s^{-1} (Graham 2004; Burchell et al. 2006; Kearsley et al. 2006). A keystone of this analog shot was provided by C. Snead (U. C. Berkeley).

Stardust Track C2092,82

Stardust track C2092,82 is 898 μm long, in an aerogel keystone (by Ron, 04/20/06, sample C2092,1,82,0,0)

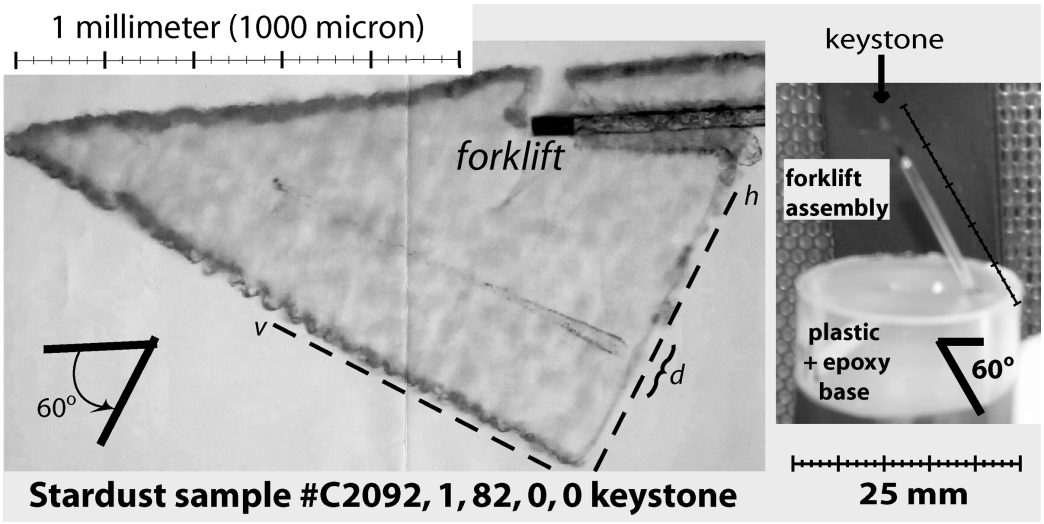

Fig. 3. Keystone and mounting apparatus. Left: Forklift is to upper right. Angle between forklift and track is ~28°. Dashed lines indicate horizontal (*h*) and vertical (*v*) planes of tomographic volumes. Notation *d* indicates entry hole depression (photo courtesy of Keiko Nakamura-Messenger, JSC, 07/06/06). Right: The glass forklift base is mounted at an angle so the track is vertical. The sample was placed in this device with a kapton window (brown colored cylinder), all in a laminar flow clean hood (Nakamura-Messenger 2007).

(Westphal 2004; Fig. 3). A mounting apparatus was made from clean plastics and epoxy, with a kapton window (Fig. 3). The sample container was opened in a laminar flow clean hood at APS. The forklift was used to mount the sample at an angle so that the track is vertical in the tomography apparatus (Fig. 3). A small (<1 mm^3) amount of plasticene clay was used to fix the glass forklift base in the hole bored in the epoxy holder base, to prevent rotation of the forklift during imaging. The kapton sleeve protecting the sample from dust was removed before run "d," to maximize information content. The sleeve was replaced immediately after the last measurement (run 'f'), before any movement of the sample. The sample was then returned to its container in the laminar flow hood.

Sample C2092,82 was imaged 22-July-2006, at 12 KeV, in three 8 h shifts to obtain five data sets at a variety of exposure times, data binning, and phase contrast, to optimize resolution and grain contrast. All images were taken using a Mitutoyo 10× microscope objective, with a 100 mm extender tube, feeding a MicroMAX 5 MHz camera. The field of view with this setup is 1.34 mm horizontal by 1.06 mm vertical, with ~1.03 μm/pixel edge with no binning of data.

Conditions were varied in (1) exposure time & binning, and (2) phase contrast (Table 1). All data were obtained using a 12 KeV X-ray beam. Ordinarily, data is collected on the 1300 × 1030 pixel CCD using 2 × 2 binning, and flat fields are collected after each 100 angles. This maximizes the signal per pixel, and reduces noise. For unbinned collection, the exposure time is roughly squared, and the number of angles must be increased (e.g., from 3 to 10 seconds from run c to run d).

Phase contrast was increased by moving the detector farther from the sample, so that beam divergence accentuated boundaries between sample regions with only subtle differences in attenuation. Three detector positions were tried: zero (minimum phase contrast, detector very close to sample), 50 mm, and 200 mm. The sample and detector geometry must be recalibrated when the detector assembly is moved.

Table 1. Runs and conditions for image sets: Binning, number of angles/180 degrees, instrumental resolution (μm/pixel edge), detector position (mm), and exposure time (s).

Run	Bin	Angles	Resolution	Detector	Exp.
b	2 × 2	720	2.06	200	3
c	2 × 2	720	2.06	0	3
d	1	900	1.023	0	10
e	2 × 2	720	2.06	50	4
f	1	900	1.03	50	12

Resolution was limited by available hardware (extension tubes, objectives), and the ability to place the objective close enough to the sample (working distance), given the location of the scintillator (Ebel and Rivers 2007). Analysis of time constraints and possible improvements led to a decision not to reconfigure the existing hardware for this work. Resolution is intrinsically limited to ~1 micron, by the wavelength of visible light, properties of the scintillator, and the accuracy of the stage motor on sample rotation. Cables for x-y sample positioning, which rotate with the upper stage assembly, were removed during runs to minimize effects on rotation. A more precise stage would eliminate some noise in sample rotation. Other groups have obtained higher resolution in synchrotron XRCMT using Fresnel zone plate (FZP) and other refinements (e.g., Nakamura et al. 2008a). Results of imaging (e.g., 900 frames at ~2500 kb/frame for "d") were

reconstructed using software parameters: normal, f = 1.25, double corr. = 1.05, averaging of flatfields, smoothing = 0, air pixels = 10, no ring removal, width = 9. Noise is present in all cases. Because noise in the reconstruction is higher in the center of images (the rotation center of the volume), the track in runs after "c" was offset 300 microns with respect to the image center.

Organic Test

Even at the low energies used here, X-rays could affect the expected organic complement of stardust particles. To test this, four glass capillaries were loaded with a polycyclic aromatic hydrocarbon (PAH) solution by Max Bernstein. This was a saturated solution of pyrene-CO_2H, pyrene-CHO, and adenine in $MeCl_2$. Capillary dimensions were: A) 0.8 mm O.D. × 32 mm long; and B) 1.6 mm O.D. × 23.5 mm long. Capillaries were dipped into the PAH solution and then solvent was allowed to evaporate, leaving a residue of PAHs on the capillary tips. One capillary from each pair (A and B) was then imaged at 12 KeV for ~35 minutes, the second capillary in each pair serving as an unexposed blank. Laser-desorption laser-ionization mass spectrometry (μL^2MS) in the laboratory of R. N. Zare at Stanford University yielded the PAH composition on the capillary tips (Kovalenko et al. 1992; Clemett and Zare 1997).

Samples were prepared by crushing the capillary ends and mounting the resulting small glass fragments onto μL^2MS sample platters using tape adhesive, which introduces no background signals. Laser desorption was performed using an Er:YAG laser (2.94 μm, 10 μm spot size); laser ionization was performed using the fourth harmonic of an Nd:YAG laser (266 nm, 4 mJ pulse energy, 2.5 ns pulse FWHM).

Laser Confocal Scanning Microscopy

We have used LCSM to study two separate keystones. The primary sample, C2092,82, (described above) is an about 1.5 μm long keystone with one large Stardust track embedded within. C2092,82 is mounted on a 25 mm "forklift" apparatus, and is stored on a machined aluminum base for storage and transport. LCSM imaging of keystones on forklifts requires dry microscopy. For analysis, the forklift apparatus was mounted transversely on a standard glass microscope slide using 2 strips of carbon tape (Fig. 4). We have since designed more robust and safe sample holders.

When using this mounting apparatus, at no point should the microscope objective come in contact with the suspended aerogel keystone. For this study, eyesight-based alignment was used, and no such contact occurred.

The keystone with analog basalt-shot track was first analyzed on its extraction forklift. It fell off, allowing us to house it within a completely closed slide and cover slip box. This protective housing enabled us to experiment with oil immersion lenses for imaging at greater magnification. Box top and bottom are #1.5 cover slips (~150 μm thick), to match the refractive index of the immersion oil.

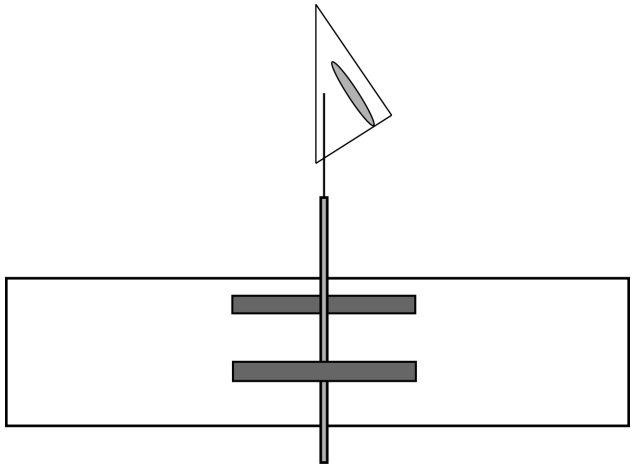

Fig. 4. LCSM Forklift mounting apparatus (not to scale).

LCSM Images were taken using a Zeiss 510 Laser Confocal Scanning Microscope at the Microscopy and Imaging Facility in the American Museum of Natural History. It is a lab bench instrument, which makes our analysis logistically simple. The instrument is equipped with 4 separate laser wavelengths for analysis: 458 nm Ar, 488 nm Ar, 543 nm HeNe, and 633 nm HeNe. All data was acquired using the 488nm Ar laser to achieve optimal resolution. Laser intensity was varied for each lens to preserve a strong reflection signal. For 10× and 20× images, the laser was kept at 20.9% and 18.9% power, respectively. This preserved the optimal balance between oversaturation of the reflection data, and underillumination of the stardust grains. Data was acquired using the 32-bit Zeiss LSM 510 v.3.2 software package (c. 1997) on a 32-bit Microsoft Windows XP computer with 4 processing cores. Data is collected in a 3-D array format X by Y by *n*, where X and Y are pixel coordinates, and *n* is the number of vertical optical slices (normal to optical axis). All scans are acquired at 2048 × 2048-pixel resolution, and *n* is varied according to the desired thickness of the analyzed region in the sample. An 8-bit grayscale depth was chosen initially to minimize data size, however subsequent work is all at 12-bit depth, to increase dynamic range of contrast.

The point of best focus in a LCSM scan is in the midplane of each optical slice, thus, all stacks of slices were overlapped 1/2 or greater thickness, in order to obtain optimal clarity. Spatial resolutions in the X and Y directions are not set equal to the slice thickness (n), for this would result in oversaturation of data, and significantly larger data sets than necessary. This procedure results in voxel elements which are not cubes, but rather rectangular prisms elongated along the optical axis. Post-processing software packages have to be adapted appropriately to handle these irregular elements.

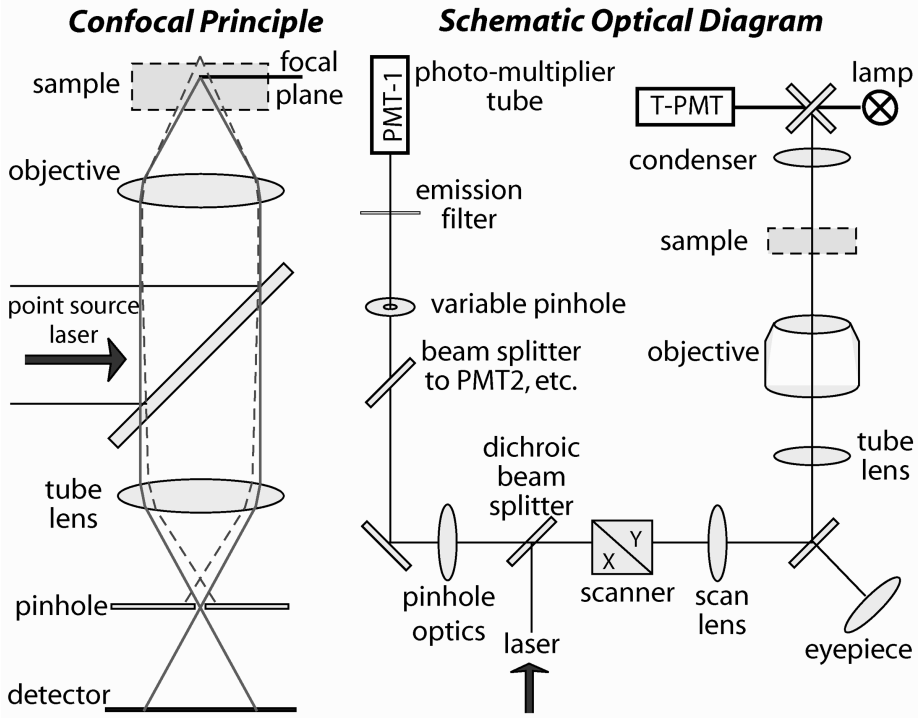

Fig. 5. Light path in the Zeiss LSM 510 Laser Confocal Scanning Microscope.

Higher resolution images were enabled with an additional digital zoom. Unlike certain types of digital zoom, the LSM 510 changes its laser scanning area, yet keeps the same scan resolution, in effect oversampling every region. The software is built to recognize elements in oversampled areas. It is important not to oversample too much, which would yield inaccurate data. Before scanning, the Nyquist theorem is applied to ensure the proper digital sampling rate is selected. The equation for the Nyquist theorem is:

$$Zoom \geq \frac{(3.92)(NA)(SystemConstant)}{(pixels)(magnification_{obj})(\lambda_{laser})}$$

Where *NA* is the numerical aperture of the lens and the System Constant for our system is 8.94 mm. This allows for scans of greater magnification without any loss of image quality. In LCSM, a pinhole is used to limit the slice thickness and limit the photons entering the detector. Our pinhole size was optimized for each magnification, but it is important to keep the pinhole size to 1.0 Airy units or below. In addition, the LSM 510 software allows for detector gain, amplifier offset, and amplifier gain modifiers. Amplifier gain, and amplifier offset were kept to ~1.0 and ~0.1 respectively, to reduce image noise. Detector gain, however, is the most effective means for changing the clarity of the images, and was therefore set low, to preserve dynamic range; this allowed for sufficiently clean and accurate images that could easily be enhanced using other software packages. The modern version (LSM 710) allows user control of these parameters over much wider dynamic ranges.

For LCSM scans of aerogel, the "VIS" (visible) setting allows for a wider field of view than the laser scans, and is useful for aligning tracks in the field of view. When changing the field of focus the objective is moving, so collision of the aerogel and objective must be avoided, and a bench mounted video camera is useful. Mapping the maximum Z (objective height) using LSM 510 software is a crucial step. Once height and spatial alignment were determined, a "quick scan" was started in "LSM" mode. Many parameters can be changed on the fly during a "quick scan" to rapidly optimize alignment and other settings. After setup, a high quality scan of a keystone could be acquired in around 6–12 hours, and a full 3-dimensional mapping of a track ~750 microns in length could be completed in about 2 days. Turnaround times for LCSM imaging are rapid, compared to synchrotron-based methods.

A scan speed (dwell time/pixel) of 3 or 4 was used, for a pixel dwell time of 12.80 µs or 6.40 µs per pixel, respectively. Longer dwell times yield higher quality images, yet below speed 4 little difference is seen. Each line of pixels was scanned twice and the values for each pixel averaged. This "line-mean-2" scan method greatly improves the clarity of images. When time is not an issue each pixel can be scanned up to 16 times, resulting in a "line-mean-16" image. Data sets are saved in Zeiss' p0oprietary LSM file format (a variation on regular TIFF stacks), and post-processed using Huygens Professional 3.0 64-bit (SVI) for 3D deconvolution, NIH ImageJ 1.41k 64-bit, and Imaris 4.5.2 64-bit for display and animation. The optical path of the LSM 510 is illustrated in Fig. 5.

Synchrotron X-ray Fluorescence

Techniques for synchrotron X-ray fluorescence analysis (SRXRF) of aerogel, and systematic errors resulting from such analyses have been described elsewhere (Borg et al. 2006; Flynn et al. 2006; Ishii et al. 2008; Lanzirotti et al. 2008). We mapped the entire length of C2092,82 at beamline 13-ID, GSECARS, Advanced Photon Source (APS), Argonne National Laboratory. An incident X-ray beam ~300 × 300 μm was focused to collect data at a resolution of ≤2 μm/pixel. Beam energy was 23 KeV, operating in top-up mode for the entirety of data collection. Three separate maps of varying sizes and resolutions were collected. First, the entire track (41454 μm^2) was mapped at 2 × 2 μm resolution, and dwell time 2 seconds per pixel. A large area of non-track material was included for later background subtraction. Two areas of high interest were then mapped in greater detail, each at a resolution of 1 × 1 μm, with dwell times of 5 and 10 seconds per pixel, respectively. For each mapped pixel, a full spectrum from 1 to 23 KeV was collected. Raw data were also binned to assess specific elements, and to analyze oversampled data.

Although SRXRF analysis is generally limited to elements with Z > 11, analyses in silica aerogel are practically limited to Z > 16. Thus relative abundances of Ca, Ti, and other lithophiles (but not Mg, Al, Si) compared to siderophile Fe, Ni, et al. must be used to distinguish between silicate/oxide assemblages and metal/sulfide assemblages.

RESULTS

XRCMT—Analog Samples

Results at 14.49 μm/pixel are shown in Fig. 6, with a focus on two tracks in shot aerogel tile. The original volume (B1) has been cropped to contain just these two tracks, particularly the one with visible dust particles in the field of view. Figure 6 shows four x-frames: x_104, x_95, and contiguous frames x_92 and x_91 that are 14.49 μm apart. Frames x_93, x_94, and x_96 to x_103 are not shown. Orthogonal z-frames (9) and y-frames (2) are also shown. The traces of selected orthogonal frames are indicated in some images (e.g., z_221 in x_104, z_406 and x_104 in y_21). Full image stacks and movies are presented in digital Appendix 1 and on the Web (Ebel www 2009).

These data allow precise 3D addressing of particular particles of interest. For example, the coordinates of one particle, in the right-most frame, are (x_104, y_21, z_406). Because volumes can be re-cut to any desired pixel dimension, the origin of these coordinates can be set to any particular feature of the aerogel tile that is easily located. For example, the z coordinates could be registered so that z_0 is the top surface of the tile. Even at 14.5 μm/pxl, however, the surface of the aerogel is not a flat surface. If the main purpose of tomography is to locate particles in 3D for computer-controlled micro-extraction (e.g., Westphal et al. 2002), it may not be advantageous to go to ultra-fine spatial resolutions, unless fiducial markings (registration) can be established with similar precision.

Several features are notable in Fig. 6. Although the top surface, visible in x- and y-frames, is bright (dense), the bulk of the aerogel is quite similar in overall intensity to the air in tracks and above the tile. Because noise in air looks like aerogel, and noise in aerogel looks like air, we have not been able to automatically threshold these two phases accurately, even though the differences are quite visible to the eye. Densification of aerogel along particle tracks is evident in brightening of images, particularly in the upper parts of the y-frames selected for Fig. 6, where tracks are widest. The best way to see these features is to import tiff image sequences into the ImageJ software and scroll through them manually (Ebel et al. 2007).

The tracks in z-frames show densification of aerogel, and also a "rifling" of the aerogel by the impacting particles, in the form of small fractures that make the holes look star-shaped. In a sequence orthogonal to *z*, these triangular embayments appear to spiral down into the aerogel in a clockwise rotation with depth. Individual embayments cannot be followed very far down *z*, and new ones appear on the way. The apparent rate of rotation of these embayments with depth may be related to the spin rate of the impacting particle.

The aerogel used here contains small particulate impurities of high atomic number. In the full images of the tile, these bright spots are visible at locations apparently unrelated to particle tracks. Extremely bright particles are noticeable, for example at (x_95, z_221) in Fig. 6, near tracks, but may *not* be part of the impacting material. We were not equipped to extract these particles for analysis.

Fragmentation of particles is evident from these images. In one place along the track (ovals, Fig. 6) it appears that part of the impactor has smeared along the wall of the track, which is narrow at this depth in the tile. Where tracks narrow, in the lower parts of x- and y-frames, densification is not evident, but more particle fragments are found. The track bifurcates at a depth of ~z_380, evident in y_21. One fragment stops at (x_104, y_21, z_406), and the other continues to z_452 (arrow in y_19). Assuming the aerogel is homogeneous, these tracks record the relative energies of the two particles. They are also likely to be particles below the spatial resolution of these images, and hints of these are visible near the bottoms of the tracks.

Volumes collected on this large slab using lambda tomography were stitched together to form a single volume, to non-destructively obtain images of the entire slab. Figure 7 illustrates combination of the *z* = 130 layer of successive image volumes B1-B5 that have been combined using stage position information. Because these are normal to *z*, they contain ring artifacts that persist during reconstruction of X-ray attenuation in the sample. In the event that an aerogel

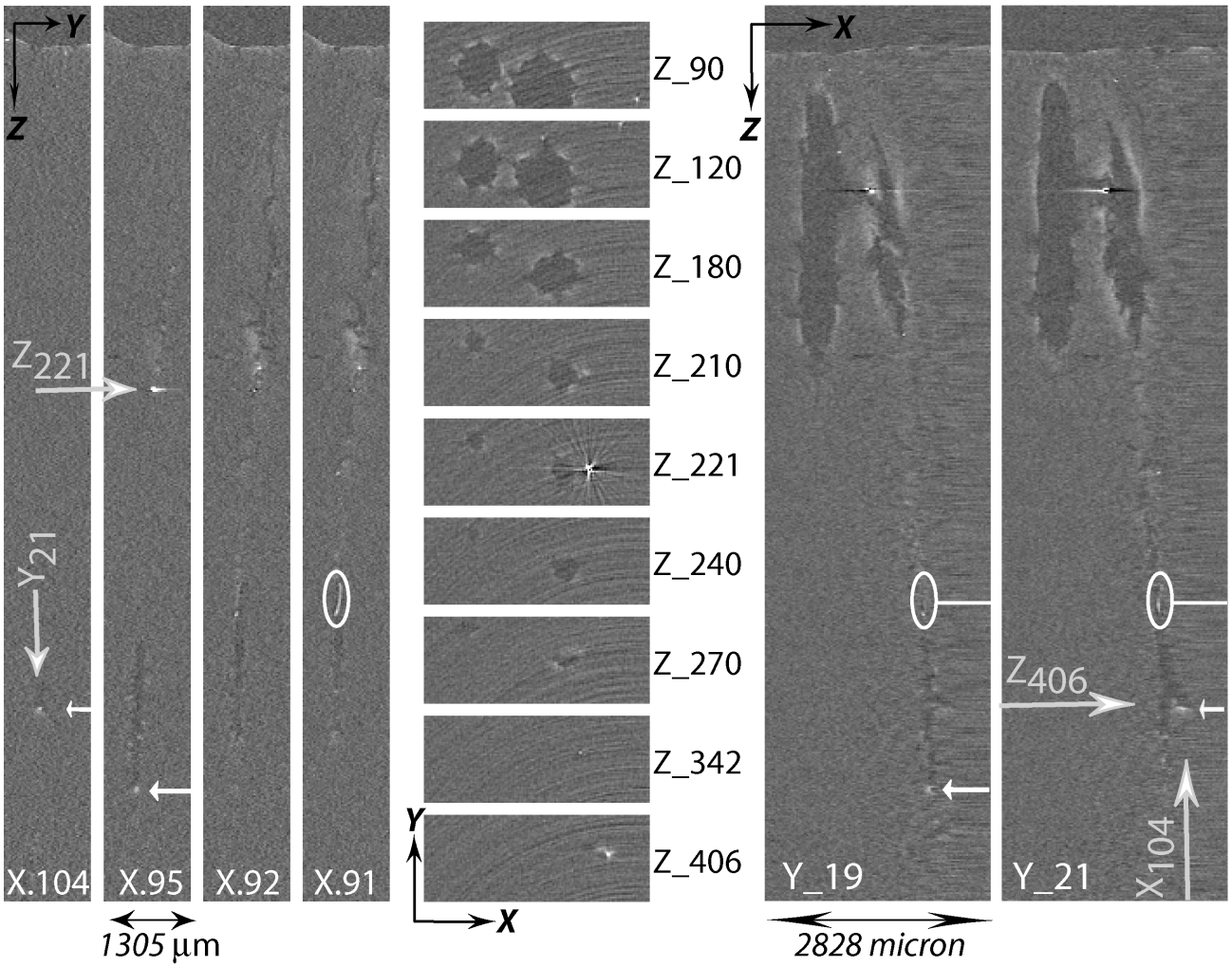

Fig. 6. Tracks and fragments in orthogonal frames. Grayscale (8-bit, 0-255) images are thresholded to the range −2500 and 4000 of original (12-bit) tomographic data. Spatial resolution 14.49 µm/pixel. Virtual slices from a volume cropped from 650 × 650 × 515 to 130 × 50 × 515 pixels.

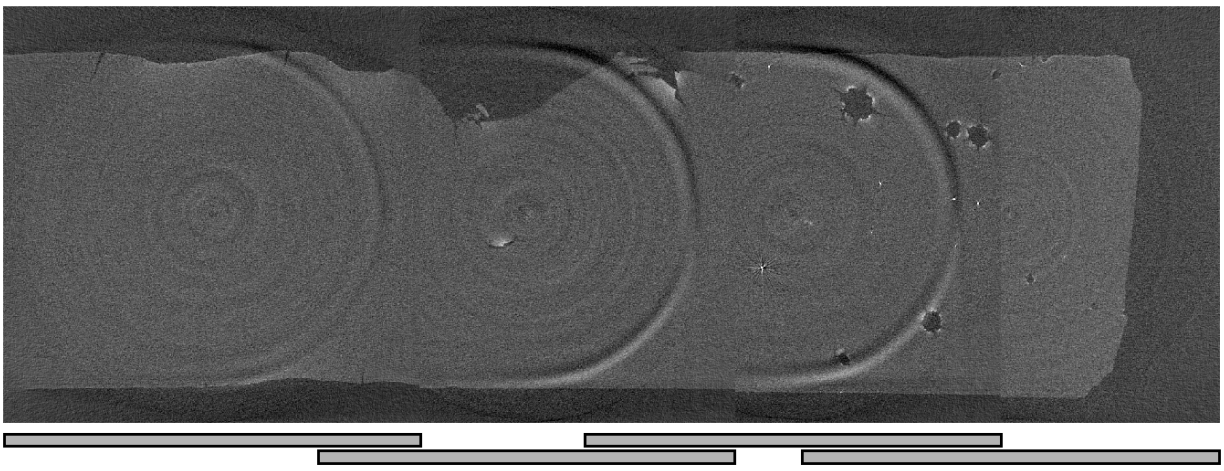

Fig. 7. Image combination in lambda-tomography. Frames are *z*-slices from adjacent volumes of the aerogel slab of Fig. 1, collected at 14.5 micron/pixel, 10 KeV.

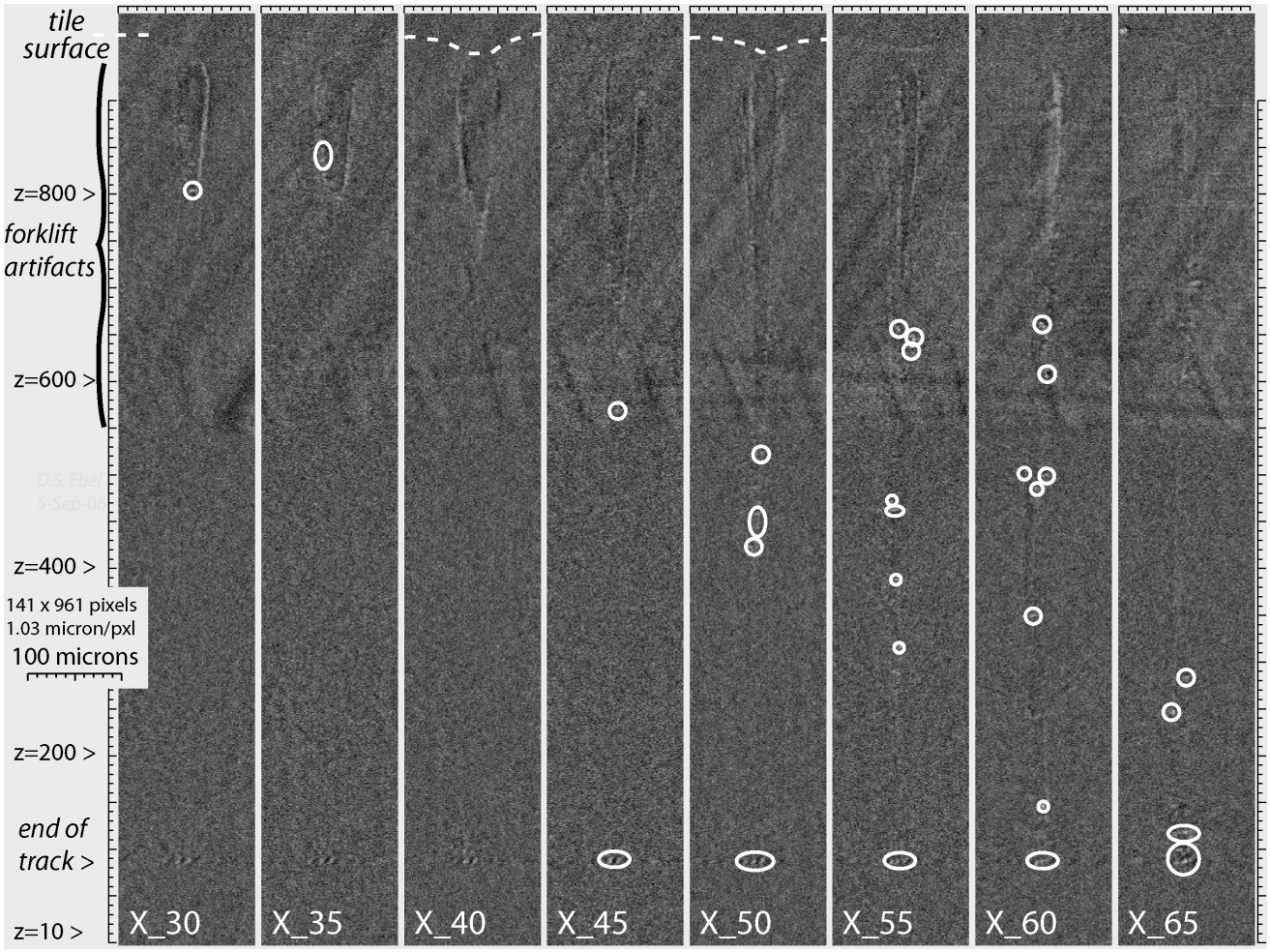

Fig. 8. Sequence of reconstructed slices on x-axis. Each fifth slice 30 through 65 is illustrated (terminal particle dominates slices 70–105). In rotating the sample, the tomography field of view includes the relatively dense glass forklift, causing artifacts in reconstruction of the aerogel+track density structure where the forklift and track are present in the same horizontal plane. In frames x_40 and x_50, dashed lines indicate inferred location of aerogel surface around the particle entry hole. Large particles are circled. (See also digital Appendix 5)

collector had many impact tracks, such imaging would allow recovery of sample locations with high accuracy.

XRCMT—Stardust Track C2092,82

Results of reconstruction are 3D data volumes with 16-bit values for X-ray attenuation (white = higher attenuation) at each volume element (voxel). Full volume files in NetCDF format are 425 MB for binned runs, and 3.4 GB for unbinned runs. The latter cannot be manipulated on a 32-bit operating system, so these volumes were cropped to contain only the track, for convenience. In run "e," for example, visual inspection establishes that the track is contained in the volume range $362 < x < 428$, $230 < y < 270$, and the full range of z. Cropping the volume to this range decreases its size by a factor of ten. Results are presented in two forms: MPG format movies, and stacks of TIF format images. The MPG files are compressed, and limited to 256 (8-bit) grayscales. The TIF files can be output as 16-bit arrays, but here considered only at 8-bit depth. Frame stacks, thresholded, are presented in Digital Appendix 2, the cropped volume is presented as Digital Appendix 3, and movies (MPG) are presented in Digital Appendix 4 (cf. Ebel-www 2009). The minimum and maximum values (thresholds) of the output data were set to optimize visibility (contrast) of tracks and particles in the aerogel. These settings do not affect the basic volume file, but apply the available output 256 grayscale range within the min/max chosen. The notation "ts1" denotes a threshold (min to max) of −1000 to +2000 within the range of the grayscale values of the raw data. All grayscale ranges are linear.

Successive slices of orthogonal C2092,82 images are illustrated in Figs. 8 and 9. Images are numbered sequentially in the cropped volume. Each successive frame is spaced from the previous frame by the resolution of the imaging (e.g., 1.03 μm for "d"), so in Fig. 8, showing every fifth frame, illustrated frames are 5.15 μm apart. The full set of images from run "d," from which Figs. 8 and 9 were taken, can be found in digital form as Digital Appendix 2 (cf. Ebel-www

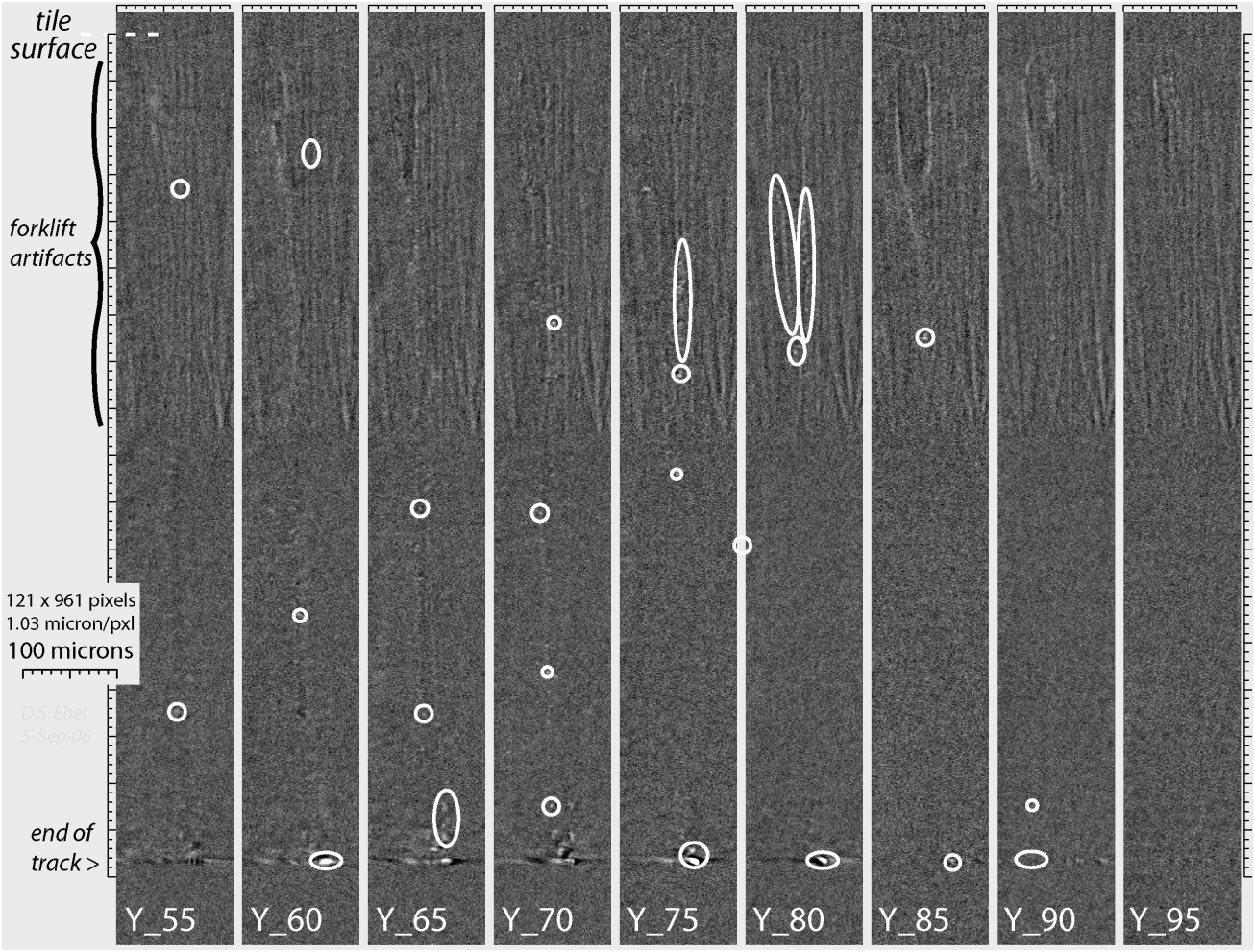

Fig. 9. Sequence of reconstructed slices on y-axis. Each fifth slice 55 through 95 is illustrated. (See also digital Appendix 5)

2009). These image sequences are conveniently viewed using the software ImageJ. A set of images at the full 16-bit grayscale resolution, or at 8-bit resolution with different thresholds, can be constructed from the volume file attached as Digital Appendix 3, using the GSECARS IDL routine "tomo_display." Note that this software may be run in the IDL "virtual machine" without purchase of an IDL license (Ebel and Rivers 2007).

In rotating the sample, the field of view includes the relatively high-density glass forklift (Fig. 3), causing artifacts where the forklift and track are present in the same horizontal plane. Image sequences normal to the sample x-axis are included as digital Appendix 5. Grains are indicated by arrows on these frames. These figures were made by importing 8-bit tif files from Appendix 2 into Adobe Illustrator, adding notation, and exporting as grayscale 150 dot-per-inch (dpi) tif format files.

Two separate terminal particles are apparent in these images. They are very close together, and there is only one stylus (thin track) leading to them. Thus the track appears to result from a single particle that broke into two at the terminus of the track.

XRCMT—Organic Tests

Simple mass spectra were measured on each PAH sample, with no major differences in mass identity and relative abundances among the four capillaries. Main peaks seen among all of the samples, and representative assignments for these peaks are:

189.2 amu—unknown

201.2 amu—pyrene with loss of one H: Formed by loss of –CHO or CO_2H from pyrene-CHO and pyrene-CO_2H, respectively. It is seen at approximately the same relative abundance in all of the samples.

218.2 amu—pyrene-OH

229.2 amu—pyrene-CHO with loss of one H or pyrene-CO_2H with loss of OH: The relative abundance of this peak does not change noticeably among the four samples.

246.2 amu—pyrene-CO_2H

A relatively small amount of pyrene-CHO (230.2 amu) was observed in the samples. No adenine was observed in any of the samples, most likely due to its small photoionization cross section at 266 nm. The μL^2MS instrument is not

Table 2. Scan conditions for imaging of C2092,82.

Scan label	Mag	*t*/µs	*r*	*n*	*t*
A-Field	10×	4/6.4	0.45	113	1.00
B-Field	20×	3/12.80	0.22	158	0.50
C-Terminal	40×	4/6.4	0.11	116	0.82
D-Entry	60×	3/12.80	0.07	199	0.34
E-Middle	40×	4/6.4	0.11	96	0.82

Table 3. Lens and zoom combinations used for LCSM imaging.

Objective	Zoom	Resolution	Pixel size
Fluar 10×/0.5	1×	2048 × 2048	0.450 µm
Fluar 20×/0.75	1×	2048 × 2048	0.225 µm
Fluar 20×/0.75	2×	2048 × 2048	0.113 µm
Fluar 20×/0.75	3×	2048 × 2048	0.065 µm
Plan-Neofluar 40×/1.3 Oil	1×	2048 × 2048	0.113 µm
Plan-Neofluar 40×/1.3 Oil	2.2×	2048 × 2048	0.052 µm
Plan-Neofluar 63×/1.0 Oil	1×	2048 × 2048	0.07 µm

particularly sensitive for highly substituted aromatic compounds. All capillaries showed the presence of small amounts of pyrene-OH. These results show that the synchrotron imaging does not change PAH-like molecules of the type used in this experiment.

LCSM—Stardust Track C2092,82

We performed several LCSM scans of varying magnification on regions of C2092,82 in its keystone. Scans of interest include two field scans of the overall region (denoted A and B), a highly magnified scan of the terminal region (C), and an extremely detailed scan of the entry point (D). In addition, scan E samples a region of particularly high material deposition in the middle of the track. Table 2 reports effective magnification (mag), scan speed/pixel dwell time (*t*/µs), pixel resolution (*r*, µm/pixel edge in x-y), number of slices (*n*), and slice thickness (*t,* µm) for each scan.

For this study, we used objective and digital zoom combinations, with resulting pixel resolution as presented in Table 3. Only a subset of these combinations was used to take published images. The best way to view resulting 3-dimensional data is through TIFF stacks or movies. Digital Appendix 6 contains examples (cf. Ebel-www 2009).

Sample projections and slice montages from the scans are presented below. Figure 10 illustrates a projection of the entire track volume onto one plane, at low resolution. In Fig. 11, the entry area is the focus, at 7 times the resolution of Fig. 10. Successive representative slices in the x-y direction are shown in Fig. 12, that are projected as a group to produce the image in Fig. 11. The fine structure resulting from aerogel-particle interactions can be explored in detail using these 3D data sets.

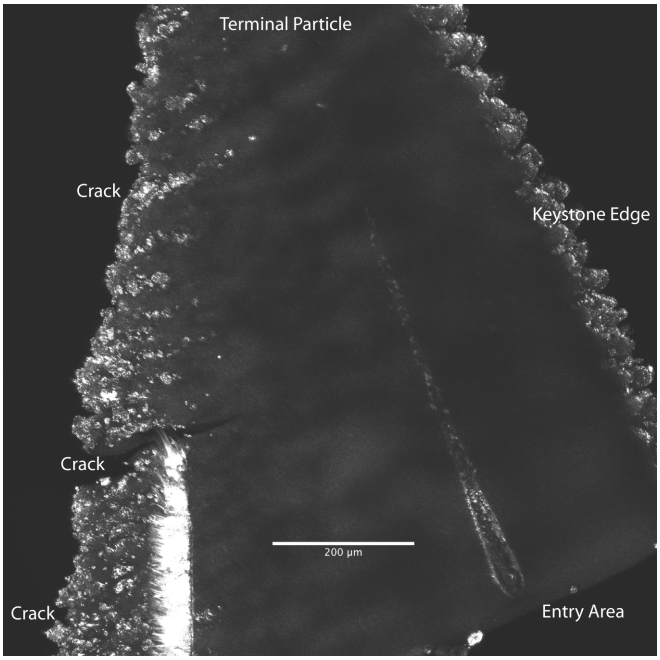

Fig. 10. Grayscale LCSM field image of C2092,82 (8 bit, 0.450 µm/pxl). Brighter areas indicate higher reflectance. The keystoning process produces strong edge effects, and the fork image (left) is oversaturated. C2092,82 extends nearly to the top of the field of view. Cracks in the aerogel result from the stress induced by the forklift apparatus (see Fig. 3).

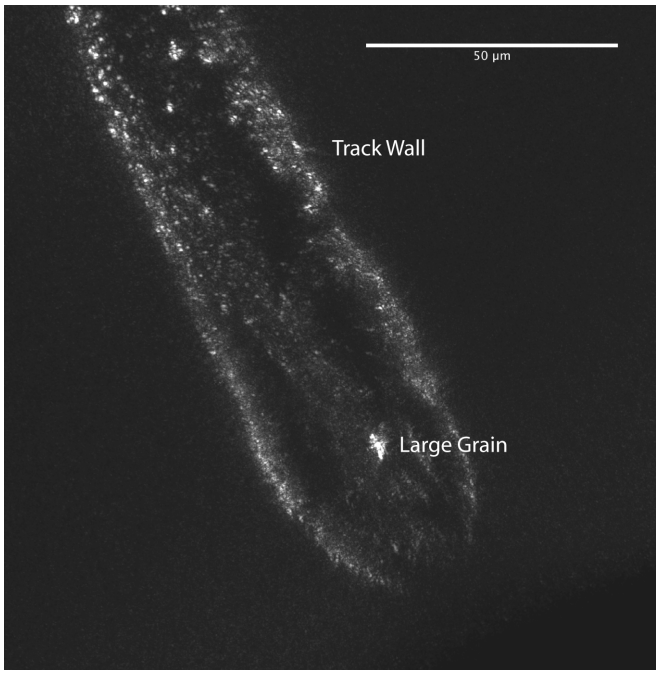

Fig. 11. Grayscale LCSM image, C2092,82, entry close-up (8 bit, 0.065 µm/pxl). Brighter areas indicate higher reflectance regions such as the track walls as well as a highly reflective particle just after the entry point. Banding on the track indicates rifling motion during impact.

LCSM—Analog Samples

LCSM scans were also taken on an analog keystone shot with basalt dust. This keystone, cut and prepared by C. Snead, is housed within a microscope slide apparatus sealed by two coverslips (Fig. 13).

This setup allowed us to image the keystone with a 40× lens to test the feasibility of using oil immersion microscopy on keystones (Table 4). The coverslip box apparatus worked flawlessly, protecting the keystone from the immersion oil, and producing no more axial distortion than an open air scan with lower power zoom lenses. Oil immersion lenses are viable for future analysis of aerogel keystones that are sealed from interaction with the oil. Pixel resolution at or better than 0.050 μm/pixel edge should be possible with our equipment (c. 1997) and techniques.

A 2D slice of a 40× scan presented in Fig. 14 illustrates a "proof of concept" that oil immersion microscopy can be used to study aerogel if the aerogel keystone is appropriately encased.

LCSM—Deconvolution

All of the track images obtained using LCSM exhibit 3D convolution artifacts, because light is diffracted around the pinhole that isolates the focal plane of each optical slice (Fig. 5). This diffraction causes brighter areas of the sample to have a pronounced distortion, or elongation of the signal along the microscope's optic axis (vertical). This 3D convolution is intrinsic to the specific optical system, including the objective as well as the optical properties of the sample itself. The scattering of light a reflector in the aerogel can be characterized mathematically by a point spread function (PSF). The PSF varies for each particular imaging configuration and sample. If one can compute an accurate PSF, deconvolution of the distorted image can be relatively simple. Computational methods of 3D deconvolution are well developed and improving. There are two major methods for computing the PSF. The first uses homogeneous spheres of known radius as models for actual points. Images of these "points" can be used directly to measure an experimental PSF. We have been unable to obtain suitably small fiducial spheres embedded in both bulk flight-grade aerogel and silica glass (proxy for melted aerogel surrounding cometary grains).

The second method, which we have used extensively here, is to calculate a theoretical PSF. We then use this PSF in an iterative deconvolution process. There are several mathematical models for 3D deconvolution, but the most appropriate for our data is the classic maximum likelihood estimation algorithm (CMLE). A much quicker, yet much less effective model, the quick maximum likelihood estimation algorithm (QMLE) was used for rapid preliminary examination of the data. The deconvolution software suite we use is Huygens Professional (SVI). Deconvolving 3D images

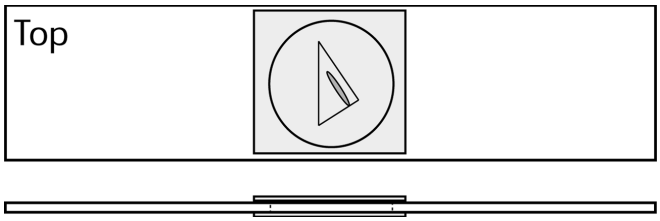

Fig. 13. Coverslip box schematic (not to scale).

Table 4. Scan parameters for oil immersion imaging of analog samples, columns as in Table 2.

Scan Label	Mag	*t*/μs	*r*	*n*	*t*
40×-Field	40×	4/6.4	0.113	188	0.31
40×-Entry	88×	6/1.6	0.052	174	0.15

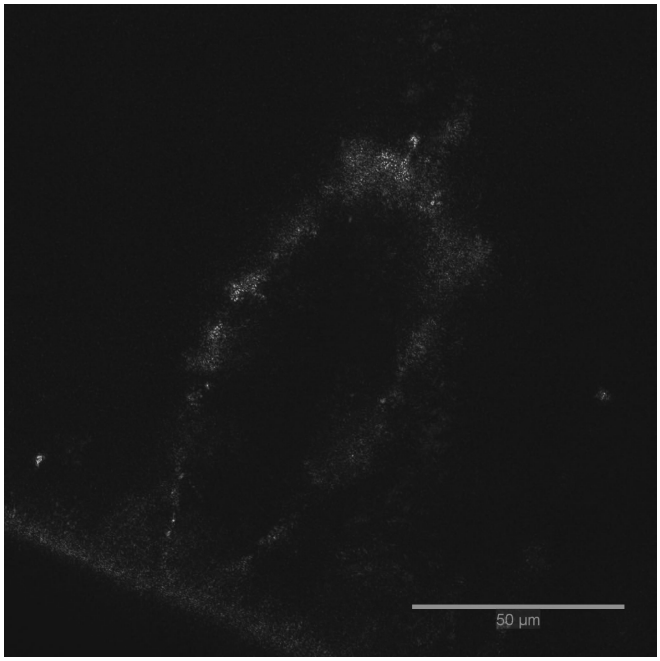

Fig. 14. LCSM image of small, type B track from basalt shot analog (8-bit). Track walls are visible in this false color representation. Brighter areas indicate areas of higher reflectance.

in Huygens is a fairly simple procedure, yet attaining accurate results requires an in-depth knowledge of the optical system. The software works by deconvolving blocks of the image stack, one at a time, and computes a quality factor for each iteration on each block. The number of blocks depends on available computer RAM. This method, while efficient, is computationally heavy and memory intensive. We determined the deconvolution parameters that give the best theoretical results, after extensive experimentation with the software. Up to 150 iterations are required to optimize the quality factor for each deconvolved block. The Huygens suite saves each deconvolved scan as a pair of ICS and IDS files, which can easily be imported into other software packages (e.g., ImageJ) using freely available plugins. We used the

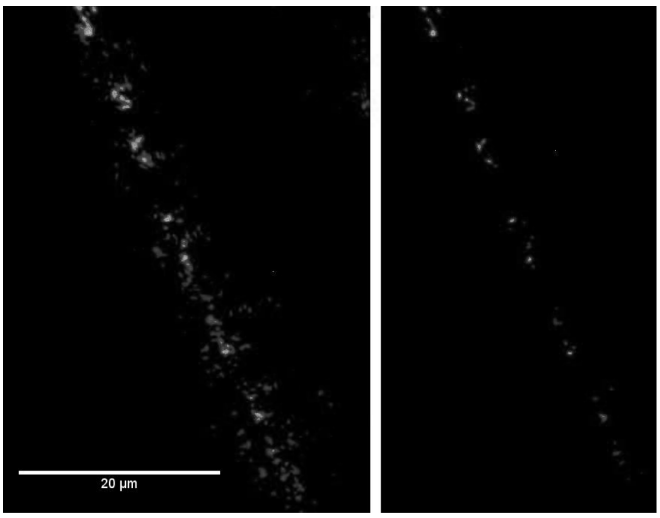

Fig. 15. Raw and deconvolved results. Unprocessed track image on the left, and properly deconvolved result is on the right. Note the minimal loss of intensity data and the large reduction in uncertainty in track wall width in the deconvolved image. These differences become most apparent in a dynamic image view, with user-controlled contrast.

Professional version of the Huygens software due to its advanced GUI and TCL scripting tools.

Properly deconvolved images are crucial to making accurate quantitative measurements from 3-dimensional LCSM image stacks. Prior to deconvolution, track boundaries identified in images have a visual uncertainty of ~4–5 μm, while properly deconvolved images have boundaries with an uncertainty of ~1 μm. This is illustrated in Fig. 15.

Reducing the visual spread of track walls allows for much greater precision in the quantitative measurement of tracks. For example, measurements of a type A track of diameter ~25 μm and length ~900 μm (similar to C2092,82) could have more than 15% error in the volume measured using data that has not been properly deconvolved. Using properly deconvolved data with a theoretical PSF cuts this uncertainty down to less than 5%. Use of a measured PSF would further decrease this uncertainty. These corrections, and, indeed, any further improvements in deconvolution, can be applied at any time after LCSM raw data collection, long after samples have been returned to the sample curation facility.

Synchrotron X-ray Fluorescence

The entirety of C2092,82 was mapped using SRXRF at 2 μm/pixel edge. A full map of raw, scaled Fe fluorescence intensity is shown in Fig. 16. The entry point is to the left. Large terminal particles (TP) and large amounts of particulate deposition in the entry area are apparent. The terminal particle is rich in Fe, Ni, Mn, and other siderophile elements, but also in Ca and Ti (Fig. 17), indicating that it is nearly chondritic in bulk (Mg, Si, Al are not analyzed). An area of high interest (A4) is rich in Ca, Ti, and Zr. This grain is worthy of extraction and detailed nanoscale analysis.

The full track map has been binned into large areas of interest in order to investigate changes in deposition chemistry as a function of track depth. These areas A1–A3 are marked by the corresponding lines in Fig. 16a. Area A4 is a sub-area of A1, highlighting particles of high interest. There is a very low signal/area ratio in the particle-poor stylus above the terminal particle (P12 to P7 to P11 in Fig. 16), and these particles are near background for all elements except iron. Presented in Table 5 are the Fe and CI normalized abundances of regions A1–A4, and for the terminal particle of C2092,82.

The abundance data for C2092,82 is consistent with and complementary to 3D confocal and tomography images. A total of ~0.35 ng of Fe was measured in C2092,82, which corresponds to ~1.92ng total cometary material, for an assumed CI elemental abundance (Lodders 2003). The terminal particle contains 91.8% of the total Fe mass, while an additional 7.9% of the Fe mass is in areas A1–A3, leaving 0.3% Fe mass in the stylus region leading up to the terminal particle. Ni and Cu are depleted compared to the CI norm in the terminal particle and steadily decrease as track depth increases. While the terminal particle is enriched in Zn compared to the CI norm, Zn abundance slowly decreases as a function of track depth as well.

Background contaminants in aerogel have been a concern in previous SRXRF studies of returned Stardust materials (Ishii et al. 2008; Lanzirotti et al. 2008). We have compensated for these effects by mapping a large area of clean background aerogel (~8000 μm^2, indicated by the white dashed line on Fig. 16b), at the same conditions as the rest of the track map. The spectra in this area were integrated and scaled to create a baseline value for background subtraction. While Si, Ar, and Br make up the largest components of the background subtracted spectra, there also exist "hot spots" with large concentrations of myriad elements. Some of these hot spots are enriched in expected cometary elements such as Fe, and Ni.

While it has been difficult for other researchers to properly identify and discard such hot spots, the combination of SRXRF with the high-resolution LCSM data allows for a nearly definitive discrimination between reflective particles in tracks and elemental anomalies (contamination) in the surrounding aerogel. Six apparent particles of high apparent Fe content (P1-P6) were identified near C2092,82. Particles rich in high-Z elements should be visible in LCSM images, but these are only barely visible. Particles P1-P6 may, therefore, be near the limit of size resolution of LCSM. They were discarded from further analysis. It is less easy, in LCSM, to see particles that appear in SRXRF to be rich in lower-Z elements, such as Ca and S. Therefore no pixels rich in these elements were discarded, so the abundances of these lower-Z elements may be due in part to hot spot contamination.

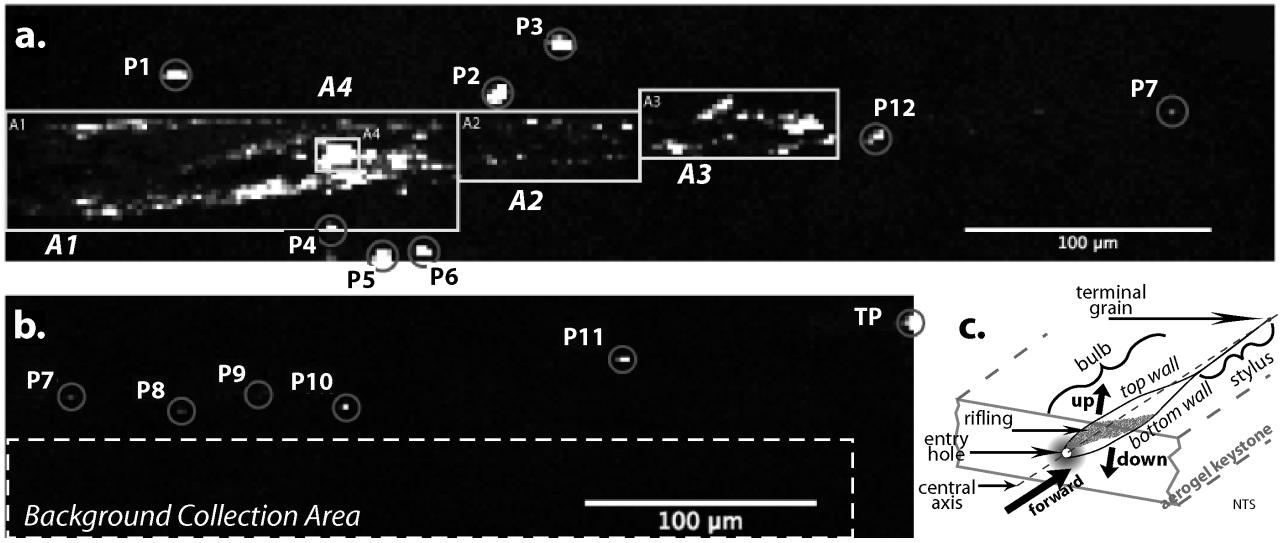

Fig. 16. Full map of C2092,82, illustrating Fe Kα fluorescence hot-spots (raw data).

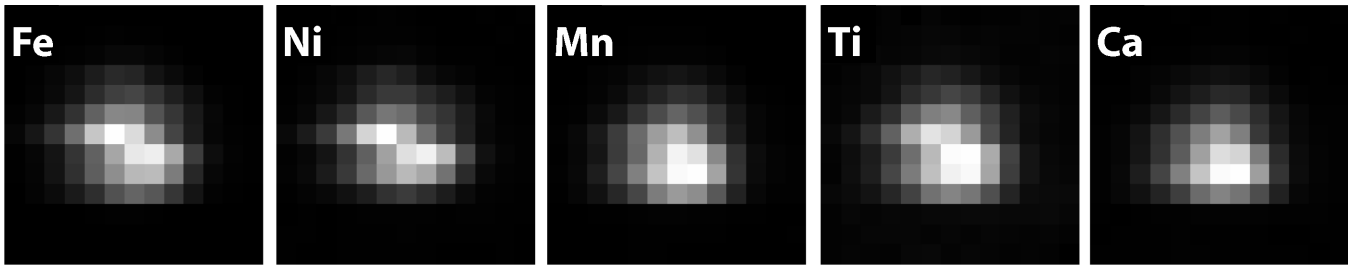

Fig 17. Fluorescence maps of 13 × 13 pixel area (1 µm/pixel) of terminal particle, C2092,82, a) Fe Kα, b) Ni Kα, c) Mn Kα, d) Ti Kα, e) Ca Kα.

Table 5. Elemental abundances (Fe and CI-normalized) in C2092,82 regions and TP.

Area	S	Ca	Cr	Mn	Fe	Ni	Cu	Zn	Zr	Ti
A1	17.63	4.64	3.28	4.30	1	2.73	167.10	175.13	1378.48	413.43
A2	3.84	0.07	8.65	9.72	1	3.16	101.56	123.74	303.30	100.63
A3	16.12	0.09	3.27	2.77	1	1.69	34.90	17.94	171.00	35.79
A4	3.09	11.14	2.30	3.67	1	2.30	382.35	338.15	3180.01	1149.82
TP	0.61	1.82	2.24	5.56	1	0.19	0.77	2.93	0.78	2.89

While LCSM is useful in confirming and rejecting particles that are apparent in the SRXRF mapping, there are also a number of particles observed in LCSM images that do not appear in the SRXRF maps. An example of one such particle is the highly reflective particle ~30 µm from the entry hole of C2092,82 (large grain, Fig. 11). This particle does not manifest itself in the SRXRF map but has the reflectance characteristic of a terminal particle. It is assumed to be a low-Z grain not detectable by XRF (Al- or Mg-rich).

DISCUSSION

XRCMT

Extreme phase contrast analysis on track C2092,82 (e.g., run "b" at 200mm) did not result in the enhanced edge effects that were expected. Phase contrast with LCSM yields much better dynamic range between in-track volumes and aerogel and densified silica. While data is usually binned 2 × 2, it was useful to collect XRCMT data without binning. Slight improvements in the resolution of track edges are apparent in comparison of runs d, e, and f. Although run "d" yields reasonably good results, without Fresnel zone plate techniques XRCMT cannot provide the resolution necessary for comprehensive, routine, rapid 3D imaging of whole Stardust tracks in translucent aerogel. In our experience, XRCMT is best suited for FZP imaging of individual opaque particles at the nm scale (e.g., Nakamura et al. 2008a). In the event that aerogel embedded samples are not translucent, XRCMT would be necessary. For translucent aerogel, the LCSM technique yields higher resolution, higher contrast images than XRCMT.

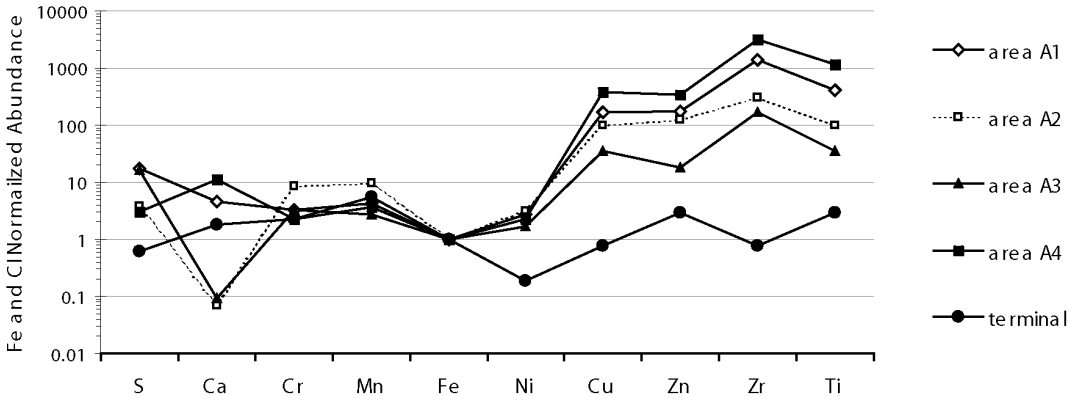

Fig. 18. Elemental abundances (Fe and CI-normalized) of major regions of C2092,82. The terminal particle appears strongly depleted in Ni and Cu compared to the rest of the track.

Infinitesimal Sample Heating in XRCMT and LCSM

Sample heating is a minor issue in aerogel tomography (XRCMT). A detailed calculation shows that sample heating is orders of magnitude smaller than heating under a standard light source, and many orders of magnitude less then under an electron microprobe beam. Here, we calculate the power deposited in a sample by a 1 μm beam at 10 keV energy. This is a maximum bound, because a significant X-ray flux passes through the keystones to the CCD. The flux of a bending magnet synchrotron source in units of photons/s/mr^2/0.1% bandwidth is:

$$\text{flux} = (1.327 \times 10^{13})^* \, E^{2*} \, I^* \, \mathbf{H}_2^* \, (e/e_c),$$

where E is the ring energy in keV (7 keV for the APS); I is the ring current in amperes (0.1 A for the APS); e is the X-ray energy; e_c is the critical energy of the accelerator (~20 keV for the APS); $\mathbf{H}_2$ is a Bessel function that has a value very close to 1.0 in the range e/e_c = 0.5 to 1.5 (i.e., 10 to 30 keV at the APS). In flux units, mr is milliradians (0.001 radians), and 0.1% bandwidth means for example 0.1 keV at 10 keV. The bandwidth of the GSECARS monochromator is about 1 eV, or about 0.01% bandwidth at 10 keV.

So at 12 keV the flux at GSECARS is approximately

$$(1.327 \times 10^{13})^* \, 7^{2*} \, 0.1^* \, 1.0^* \, (12/20)^* \, (0.1) \cong 3.25 \times 10^{12} \text{ photons/s/mr}^2$$

where the last 0.1 corrects for a bandwidth of 0.01% versus 0.1%. The tomography station is ~50 m from the X-ray source. For a 1 mm beam, the angular size is (1 mm/50 m)^2 = 4×10^{-4} mr^2. Thus the flux in a 1 mm^2 beam is $(6.5 \times 10^{12})^*(4 \times 10^{-4})$ = (2.6×10^9) photons/s/mm^2. This flux of photons at 10 keV = 2.6×10^9 photon/s* 10 keV/photon = 2.6×10^{10} keV/s. Converting this flux to power we have 1 keV = 10^3eV = 10^{3*} 1.602177×10^{-19} joule/eV = $1.6*10^{-16}$ joule. Thus, the power in a 1 mm^2 beam in the tomography station is 2.6×10^{10} keV/s* 1.6×10^{-16} joule/keV = 4.2×10^{-6} joule/s = 4.2×10^{-6} Watts.

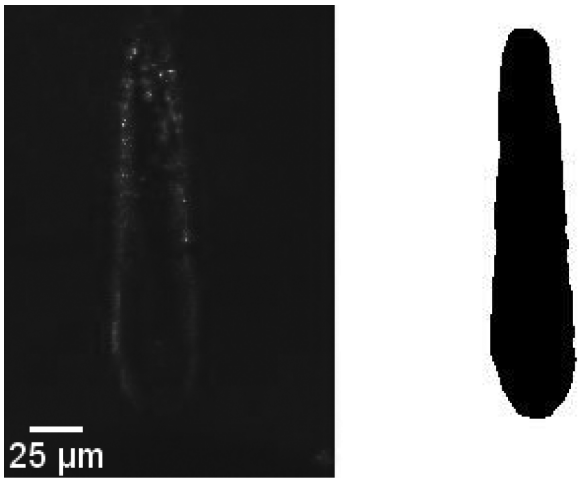

Fig. 19. Partial slice of C2092,82 (left), and corresponding manually outlined shape (right).

Assuming all power is absorbed in the sample and none is transmitted, the power being deposited by the X-ray beam is 4.2 micro-watts per square mm. This is a very low power density. If the beam intercepted 1 cm^2 of sample, then the power would be 4.2×10^{-4} W, or 1.0×10^{-4} calories/s. If this were absorbed in a 1 cm thick sample of water (1 cm^3), the water would heat up by 0.0001 degrees/s (~1° in 3 hours) if there were no heat loss. This power density can be compared to an electron microprobe. An electron microprobe running at 10 keV, at 100 micro-amps has a power of 10^{-3} W. If this power is deposited in 1 μm^2, the power density is 10^3 W/mm^2. Thus, the electron probe beam has more than 200 times the total power of a 1mm synchrotron X-ray beam, and the power density ratio is $(10^3$ W/mm$^2)/(4.2 \times 10^{-6}$ W/mm$^2)$ = 2.2×10^8, or more than 100 million times higher. The power of 4.2×10^{-4} W/cm^2 can also be compared to the power from a 60 W fiber optic light source which can almost certainly deposit several watts of power in a 1 cm^2 field of view, thousands of times higher than the X-ray beam. It has been

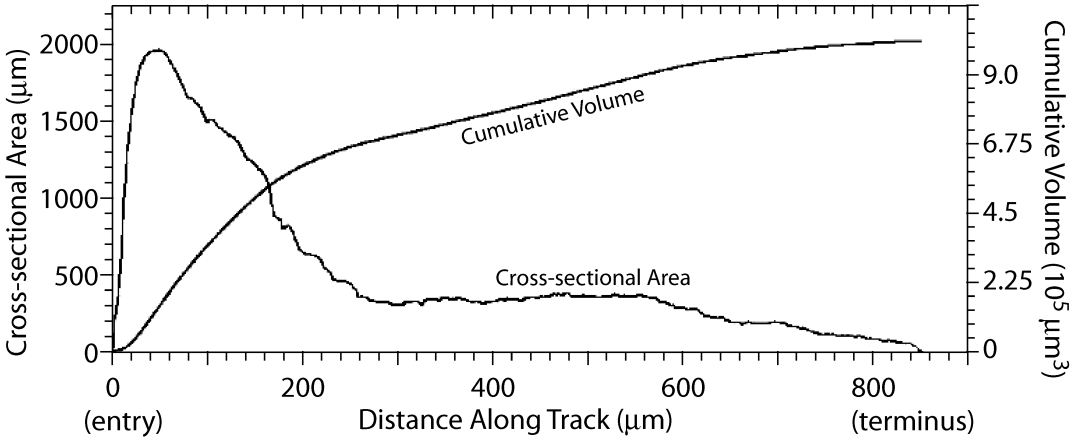

Fig. 20. Profiles of C2092,82: cross sectional area and cumulative volume. Cross sectional area seems to taper off in a 1/n fit.

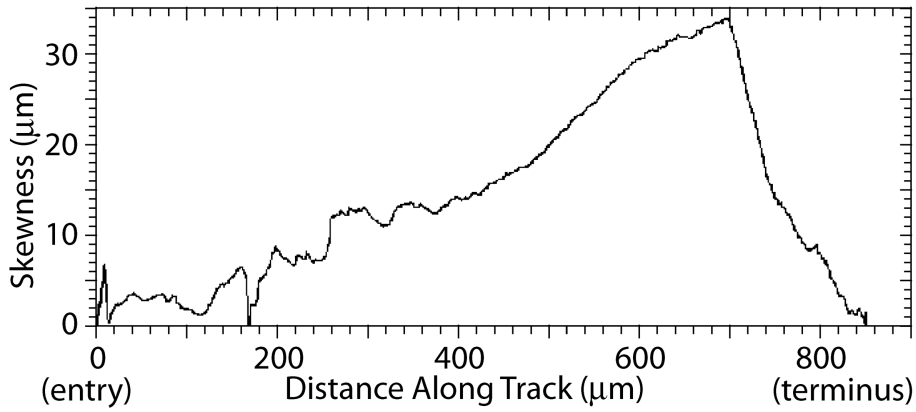

Fig. 21. Absolute skewness from direct path, calculated for C2092,82.

shown elsewhere (Denk 1995, pp. 450) that sample heating is not an issue in LCSM study of biological materials.

LCSM Quantitative Analysis

After acquisition and post-processing, the LCSM images were subjected to 3-D numerical analysis. We were not able to adapt image processing algorithms to automatically distinguish the edges of the molten aerogel from the central cavity of each track, so tracks were outlined (segmented) by hand at high magnification using the open-source program ImageJ v.1.42. This process yielded highly accurate slice-by-slice outlines of tracks. Figure 19 illustrates a portion of a LCSM slice and its corresponding outline.

Segmented tracks were thresholded, resulting in binary TIFF stacks. These were read into custom IDL routines that calculated cross sectional area and cumulative track volume as a function of z slice (Fig. 20), and a skewness profile (Fig. 21). Our skewness profile was calculated as the 3-dimensional distance between the centroid of each serial z slice and a reference straight line from the center of the entry point to the center of the terminal particle (Fig. 16c). Skewness is defined as

$$X_{skew}(z) = X_{cog,z} - \frac{(X_{cog,t} - X_{cog,e})(N - Z_e)}{(Z_t - Z_e)} + X_{cog,e}$$

$$Y_{skew}(z) = Y_{cog,z} - \frac{(Y_{cog,t} - Y_{cog,e})(N - Z_e)}{(Z_t - Z_e)} + Y_{cog,e}$$

where subscripts *cog* indicate coordinates of the center of gyration, for the entry region (subscript *e*), and the terminal area (subscript *t*), and *N* is the number of serial z slices. Skewness can be calculated in the X and Y directions, as above, and as an absolute skewness as a function of z:

$$Skew(z) = \left[X_{skew}(z)^2 + Y_{skew}(z)^2\right]^{\frac{1}{2}}$$

Track Morphology and Particle Fragmentation History

Every Stardust grain is the product of a complex interaction between an original Wild 2 particle and the aerogel collector. Track C2092,82 is, therefore, a timeline of

aerogel-comet particle interaction. It is possible through a combination of 3D LCSM image data and complementary XRF chemical data to describe in detail the original particle's fragmentation history and ascribe causes to particular features of track morphology. Upon impact, the original particle pulled on the aerogel surface, creating a 20 μm deep, curved divot ~140 μm in diameter (Fig. 10, LCSM image). Thus the 15.5 μm entrance hole is recessed 20 μm from the original aerogel surface, shortening the effective length of the track. The first 30 μm of C2092,82 is marked by a very slightly curved streak of deposited fine material on the top track wall, which can be seen in both the LCSM images and XRF maps. At 30 μm in, a large grain (2 × 2 μm) was deposited on the bottom of the track, opposite the streak of fine material (Fig. 16c). This grain is highly reflective in LCSM, yet does not appear in the XRF maps, which may indicate a mineralogy rich in low-Z elements (e.g., Mg, Si, Al). The deposition of this grain is the apparent cause of the increased rotational velocity of the main particle, inferred by rifling textures on track walls. Rotation speed and direction can be inferred from measurements of the rifling texture (cf. Nakamura-Messenger et al. 2007).

After deposition of the large grain at 30 μm, a streak of fine deposited material makes a 90 degree rotation in 59 μm of forward travel, and it can be inferred that 180 degrees of rotation at this rate is achieved in <120 μm of travel. A large amount of deposited material on the top wall of the track (Fig. 16) appears in both the LCSM and XRF data, 145 μm into the track, and ~115 μm beyond deposition of the first large grain, deposited on the bottom of the track. We infer that both the first grain and the many grains, some larger than the first grain, deposited 145 μm beyond the entry hole were deposited from the same side of the original particle, which had a constant rotational velocity. The deposition of this large amount of material appears to have strongly affected the particle trajectory, skewing the track 15 degrees off its original vector (toward the "bottom" in Fig. 16), consistent with conservation of angular momentum. The highly refractory, high-Z nature of this material (XRF region A4 in Fig. 16) indicates that it may be complementary to the first large grain, if the entire original particle was chondritic in bulk composition. Additionally, the large effect on track geometry correlated with this deposition event leads us to think that more mass may be deposited in this location than is indicated by the XRF data. XRF-based mass calculations are grounded in CI-normalized values, which may not be an appropriate assumption for grains deposited in this area (Fig. 16). Similar logic applies to grain P11, which coincides with an abrupt change in calculated skewness (Fig. 21, at x ~ 380 px). Particle P11 accounts for <0.1% of total mass by Fe-content.

The fragmentation history inferred here corresponds to 150 μm of track (XRF section A1, Fig. 16) and accounts for 5.9% of the total cometary material deposited. The terminal grain of C2092,82 contains 91.8% of the total material, leaving 2.3% of total mass in the remaining ~700 μm before the terminal grain. This explains the barren appearance of this region in both the LCSM and XRF data. Rotational velocity beyond region A1 is difficult to determine due to this lack of deposition, although the deposition profile of the largest particles in regions A2 and A3 appears to alternate between the top and bottom of the track at regular intervals. In the region leading up to the terminal particle, beyond region A3 (Fig. 16), only five grains are observed, indicating that the original particle had shed all but its most tightly bound material.

We infer that the original particle that formed track C2092,82 was a conglomerate of materials comprising a largely chondritic core (>90%), one side covered by loosely aggregated very fine material, and the other side by loosely aggregated, coarser material, with discrete, low-Z particles (e.g., Mg_2SiO_4) and more refractory, high-Z particles. The disaggregation of the majority of the loose materials (region A1) was probably caused by either the release of volatiles from the original particle, or the shock waves produced during hypervelocity capture as discussed by Trigo-Rodriguez et al. (2008). The combination of LCSM and XRF data, combined with advances in hypervelocity impact modeling (e.g., Dominguez 2009; Anderson 1998), and laboratory calibrations (e.g., Burchell et al. 2008) will allow more rigorous, quantitative investigation of particle capture dynamics.

CONCLUSIONS

We have compared high resolution 3rd-generation synchrotron XRCMT imaging with LCSM imaging using the Zeiss LSM 510 instrument. It might be possible to extract better information from XRCMT by combining data at different phase contrasts. We show by experiment that XRCMT is nondestructive of PAH-like organic compounds. Compared to LCSM, however, synchrotron microtomography does not provide high spatial resolution and low noise without zone plate techniques and very accurate (piezo) stage controls not present in many beamline configurations. We have demonstrated routine use of LCSM for non-destructive submicron 3D analysis of grains and tracks in aerogel returned by the Stardust mission. Critical to this method is the newly developed ability to reduce distortion inherent in the raw LCSM results through 3D deconvolution. LCSM provides <100 nm/pixel horizontal, and ~2.5× that in vertical (along optic axis) resolution in a benchtop instrument (c. 1997). LCSM allows precise quantitative volumetric analysis of the results of the kinetic interaction between incoming comet particles and the aerogel target, in measures of volume, concentricity and skewness along tracks. We have combined LCSM images of micron-sized grains in the <1 mm length Stardust track C2092,82 with SRXRF chemical maps to

identify grains of interest for detailed analysis, and to quantify the chemical composition of this track. This combination allows rejection of aerogel contaminant concentrations. We find correlations between chemical composition and track depth, and calculate bulk chemical properties of whole tracks. The XRF data tells us where non-aerogel material is located, but is limited in analyzable elements. The LCSM imaging reveals possible mass concentrations because 3D track geometry is correlated with mass deposition by laws of energy conservation. Combined LCSM + SRXRF analysis is thus yielding chemical, textural, and physical information on Stardust tracks at the highest possible resolution without apparent or measurable destruction (e.g., of surviving organic matter). The picokeystones containing interstellar (IS, Westphal 2009) dust are excellent candidates for non-destructive LCSM analysis.

Acknowledgments–Fred Hörz provided shot aerogel, the key samples. Mike Zolensky encouraged this work, in preparing for worst case scenarios for sample return. George Flynn, Andrew Westphal, Steve Sutton, Mark Burchell and Anton Kearsley provided advice along the way. Dr. Jon Friedrich, and students Antonio Buono, John Bigolski, and Hugo Rodriquez helped at the beamline. Rebecca Rudolph and Emily Griffiths started us on the LCSM 510. This research has made use of NASA's Astrophysics Data System Bibliographic Services. Use of the APS was supported by the U.S. Department of Energy, Office of Science, Office of Basic Energy Sciences, under Contract No. W-31-109-ENG-38. This work was supported by the American Museum of Natural History, and National Aeronautics and Space Administration grants NAG5-12855 and NNC066E42G (DSE).

Editorial Handling—Dr. John Bradley

REFERENCES

Anderson W. W. 1998. Physics of interplanetary dust collection with aerogel. NASA STI/Recon Technical Report N.98. 97922.

Borg J., Djouadi Z., Grossemy F., Eichert D., Martinez-Criado G., Westphal A. J., Deboffle D., Snead C. J., and Somogyi A. 2006. Synchrotron X-rays in situ analysis of extraterrestrial grains trapped in aerogel. *Advances in Space Research* 38:2068–2074.

Burchell M. J., Graham G., and Kearsley A. 2006. Cosmic dust collection in aerogel. *Annual Reviews of Earth and Planetary Science* 34:385–418.

Burchell M. J., Fairey S. A. J., Wozniakiewicz P., Brownlee D. E., Hörz F., Kearsley A. T., See T. H., Tsou P., Westphal A., Green S. F., Trigo-Rodríguez J. M., and Dominguez G. 2008. Characteristics of cometary dust tracks in Stardust aerogel and laboratory calibrations. *Meteoritics & Planetary Science* 43:23–41.

Clemett S. J. and Zare R. N. 1997. *Molecules in astrophysics: Probes and processes*, edited by Dishoeck E. F. von. Leiden, The Netherlands: Kluwer Academic Publishers. pp. 305–320.

Denk W., Piston D. W., and Webb W. W. 1995. Two photon molecular excitation in laser-scanning microscopy. In *Handbook of biological confocal microscopy*, 2nd ed., edited by Pawley J. B. New York: Plenum Press. pp. 445–458.

Dominguez G. 2009. Time evolution and temperatures of hypervelocity impact generated tracks in aerogel. *Meteoritics & Planetary Science* 44. This issue.

Ebel D. S. and Rivers M. L. 2007. Meteorite 3-dimensional synchrotron microtomography: Methods and applications. *Meteoritics & Planetary Science* 42:1627–1646.

Ebel D. 2009. http://research.amnh.org/users/debel/stardust/aerogel1.html.

Flynn G. J., Bleuet P., Borg J., Bradley J., Brenker F., Brennan S., Bridges J., Brownlee D. E., Bullock E., Clark B. C., Dai Z. R., Daghlian C., Djouadi Z., Fakra S., Ferroir T., Floss C., Franchi I., Gainsforth Z., Gallien J.-P., Gillet Ph., Grant P. G., Graham G. A., Green S., Grossemy F., Heck P., Herzog G. F., Hoppe P., Hörz F., Huth J., Ignatyev K., Ishii H., Joswiak D., Kearsley A. T., Khodja H., Lanzirotti A., Leitner J., Lemelle L., Leroux H., Luening K., MacPherson G., Marhas K., Marcus M., Matrajt G., Nakamura T., Nakano T., Newville M., Papanastassiou D., Pianetta P., Rao W., Rietmeijer F., Rost D., Schwandt C., See T., Sheffield-Parker J., Simionovici A., Sitnitsky I., Snead C., Stadermann F., Stephan T., Stroud R., Susini J., Suzuki Y., Sutton S., Taylor S. R., Teslich N., Troadec D., Tsou P., Tsuchiyama A., Uesugi K., Westphal A., Wozniakiewicz P., Vicenzi E., Vincze L., and Zolensky M. E. 2006. Elemental compositions of comet 81P/Wild 2 samples collected by Stardust. *Science* 314:1731–1735.

Graham G. A., Kearsley A. T., Butterworth A. L., Bland P. A., Burchell M. J, McPhail D. S., Chater R., Grady M. M., and Wright I. P. 2004. Extraction and microanalysis of cosmic dust captured during sample return missions: Laboratory simulations. *Advances in Space Research* 34:2292–2298.

Ishii H. A. Brennan S., Bradley J. P., Luening K., Ignatyev K., Pianetta P. 2008. Recovering the elemental composition of comet Wild 2 dust in five Stardust impact tracks and terminal particles in aerogel. *Meteoritics & Planetary Science* 43:215–232.

Kearsley A. T., Burchell M. J., Hörz F., Cole M. J., and Schwandt C. S. 2006. Laboratory simulation of impacts on aluminum foils of the Stardust spacecraft: Calibration of dust particle size from comet Wild 2. *Meteoritics & Planetary Science* 41:167–180.

Kearsley A. T., Ball A. D., Graham G. A., Burchell M. J., Ishii H., Cole M. J., Wozniakiewicz J., Hörz F., and See T. H. 2007. Aerogel Track morphology: Measurement, three dimensional reconstruction, and particle location using confocal laser scanning microscopy (abstract #1690). 38th Lunar and Planetary Science Conference. CD-ROM.

Kovalenko L. J., Maechling C. R., Clemett S. J., Philippoz J. M., Zare R. N., and Alexander C. M. O. 1992. Microscopic organic analysis using two-step laser mass spectrometry: application to meteoritic acid residues. *Analytical Chemistry* 64:682–690.

Lanzirotti A., Sutton S. R., Flynn G. J., Newville M., and Rao W. 2008. Chemical composition and heterogeneity of Wild 2 cometary particles determined by synchrotron X-ray fluorescence. *Meteoritics & Planetary Science* 43:187–214.

Lodders K. 2003. Solar system abundances and condensation temperatures of the elements. *The Astrophysical Journal* 591:1220–1247.

Nakamura-Messenger K., Zolensky M. E., Bastien R., See T. H., Warren J. L., Bevill T. J., Cardenas F., Vidonic L. F., Hörz F., McNamara K. M., Allen C. C., Westphal A. J., Snead C., Ishii H. A., and Brownlee D. 2007. Stardust curation at Johnson Space Center: Photo documentation and sample processing of submicron dust samples from comet Wild 2 for meteoritics science community. (abstract #2191) 38th Lunar and Planetary Science Conference. CD-ROM.

Nakamura T., Tsuchiyama A., Akaki K., Uesugi T., Nakano T., Takeuchi A., Suzuki Y., and Noguchi T. 2008a. Bulk mineralogy

and three-dimensional structures of individual Stardust particles deduced from synchrotron X-ray diffraction and microtomography analysis. *Meteoritics & Planetary Science* 43: 233–246.

Nakamura T., Noguchi T., Tsuchiyama A., Ushikubo T., Kita N. T., Valley J. W., Zolensky M. E., Kakazu Y., Sakamoto K., Mashio E., Uesugi K., and Nakano T. 2008b. Chondrule-like objects in short-period comet 81P/Wild 2. *Science* 321:1664–1667.

Potts P., Thompson M., Wilson S., and Webb P. 2005. G-Probe-2—An international proficiency test for microbeam laboratories—Report on round 2/May 2005 (NKT-1G Basaltic Glass) *Geostandards Newsletter*.

Sutton S. R. 2006. User research facilities in the earth sciences. *Elements* 2:7–8.

Trigo-Rodríguez J. M., Dominguez G., Burchell M. J., Hörz F., and Llorca J. 2008. Bulbous tracks arising from hypervelocity capture in aerogel. *Meteoritics & Planetary Science* 43:75–86.

Tsou P., Brownlee D. E., Sandford S. A., Hörz F., and Zolensky M. E. 2003. Wild 2 and interstellar sample collection and Earth return. *Journal of Geophysical Research*, 108, E10, doi:10.1029/2003JE002109.

Tsuchiyama A., Nakamura T., Okazaki T., Uesugi K., Nakano T., Sakamoto K., Akaki T., Iida Y., Jogo K., and Suzuki Y. 2009. Three-dimensional structures and elemental distributions of Stardust impact tracks using synchrotron microtomography and X-ray fluorescence analysis. *Meteoritics & Planetary Science* 44:1203–1224.

Tuzzolino A. J., Economou T. E., Clark B. C., Tsou P., Brownlee D. E., Green S. F., McDonnell J. A. M., McBride N., and Colwell M. T. S. H. 2004. Dust measurements in the coma of comet 81P/Wild 2 by the dust flux monitor instrument. *Science* 304:1776–1780.

Westphal A. J., Snead C., Borg J., Quirico E., Raynal P-I., Zolensky M. E., Ferrini G., Colangeli L., and Palumbo P. 2002. Small hypervelocity particles captured in aerogel collectors: Location, extraction, handling and storage. *Meteoritics & Planetary Science* 37:855–865.

Westphal A. J., Snead C., Butterworth A., Graham G. A., Bradley J. P., Bajt S., Grant P. G., Bench G., Brennan S., and Pianetta P. 2004. Aerogel keystones: Extraction of complete hypervelocity impact events from aerogel collectors. *Meteoritics & Planetary Science* 39:1375–1386.

Westphal A. J., Allen C., Bajt S., Basset R., Bastien R., Bechtel H., Bleuet P., Borg J., Brenker F., Bridges J., Brownlee D. E., Burchell M., Burghammer M., Butterworth A. L., Cloetens P., Cody G., Ferroir T., Floss C., Flynn G. J., Frank D., Gainsforth Z., Grun E., Hoppe P., Kearsley A., Lemelle L., Leroux H., Lettieri R., Marchant W., Mendez B., Nittler L. R., Ogliore R., Postberg F., Sandford S. A., Schmitz S., Silversmit G., Simionovici A., Srama R., Stadermann F., Stephan T., Stroud R. M., Susini J., Sutton S., Trieloff M., Tsou P., Tsuchiyama A., Tyliczszak T., Vekemans B., Vincze L., Warren J., and Zolensky M. E. 2009. Stardust interstellar preliminary examination (ISPE) (abstract #1786). 40th Lunar and Planetary Science Conference. CD-ROM.

Zolensky M. E., Zega T., Yano H., Wirick S., Westphal A., Mike K., Iris Weber I., Warren J. L., Velbel M., Tsuchiyama A., Tsou P., Toppani A., Tomioka N., Tomeoka K., Teslich N., Taheri M., Susini J., Stroud R., Stephan T., Stadermann F., Snead C., Simon S., Simionovici A., See T., Robert F., Rietmeijer F., Rao W., Perronnet M., Papanastassiou D., Okudaira K., Ohsumi K., Ohnishi I., Nakamura-Messenger K., Nakamura T., Mostefaoui S., Mikouchi T., Meibom A., Matrajt G., Marcus M.,Leroux H., Lemelle L., Le L., Lanzirotti A., Langenhorst F., Krot A., Keller L., Kearsley A., Joswiak D., Jacob D., Ishii H., Harvey R., Hagiya K., Grossman L., Grossman J., Graham G., Gounelle M., Gillet P., Genge M., Flynn G., Ferroir T., Fallon S., Ebel D., Dai Z.-R., Cordier P., Clark B., Chi M., Butterworth A., Brownlee D., Bridges J., Brennan S., Brearley A., Bradley J., Bleuet P., and Bland P., and Bastien R. 2006. Mineralogy and petrology of comet 81P/Wild 2 nucleus samples. *Science* 314: 1735–1739.

APPENDIXES

Available at http://research.amnh.org/users/debel/stardust/aerogel1.html.

Digital Appendix 1. Full tomography image stacks, Allende-shot analog slab run B1.

Digital Appendix 2. Tomography frame stacks of C2092,82, run “d.”

Digital Appendix 3. Cropped tomography volume, thresholded, C2092,82.

Digital Appendix 4. Tomography data as movies through C2092,82.

Digital Appendix 5. Annotated tomography image stack normal to x, C2092,82, run “d.”

Digital Appendix 6: LCSM image stacks of C2092,82.